LASER & PHOTONICS REVIEWS
www.lpr-journal.org

Handheld Embedded Laser-Diode Illumination Optoacoustic System for Real-Time 3D Angiography of Deep Tissues

Xiang Liu, Federico Villani, Isaac Esteban, Xuyang Chang, Baoyuan Zhang, Andrea Cossettini, Xosé Luís Deán-Ben, Luca Benini, and Daniel Razansky**

The clinical adoption of optoacoustic imaging is currently being impeded by the bulky design and high cost of traditional systems based on solid-state lasers. We introduce a cost-effective, high-performance Handheld Embedded Laser-diode Illumination Optoacoustic System (HELIOS) based on a spherical array probe incorporating a compact illumination source located in close proximity to the imaged object. High performance drivers have been designed to produce 1.8 mJ energy pulses at 915 nm wavelength, sufficient for rendering entire ≈1 cm^3 image volumes with high spatial and temporal resolution. The fast imaging performance is further facilitated by high-speed acquisition electronics capable of simultaneous sampling of all 256 transducer channels, thus enabling volumetric imaging at up to 400 Hz frame rate corresponding to pulse repetition frequency of the laser diodes. HELIOS attains image quality and performance metrics on par with those achieved with solid state laser sources. We then demonstrate real-time volumetric angiography of human fingers and palm in a freehand mode, perform large-scale volumetric compounding of vascular structures from the time-lapse 3D data, and visualize vessel perfusion and pulsation with the system. The work represents a major leap toward the translation of optoacoustics into point-of-care diagnostics and enabling its dissemination in resource-limited settings.

1. Introduction

Following nearly two decades of extensive preclinical investigations,[1–8] recent clinical trials have corroborated the immense diagnostic potential of optoacoustic (OA) imaging across a wide range of indications, including cardiovascular[9–12] and cerebrovascular [13,14] diseases, oncology,[15–20] dermatology,[21,22] inflammatory diseases,[23,24] among others.[25] Presently, most clinical OA systems rely on bulky and expensive solid-state laser (SSL) sources [26]; hence, a pressing need exists for the development of compact, cost-effective, and practical OA systems to facilitate portability and widespread clinical adoption of this technology.

The use of alternative light sources, such as light-emitting diodes (LEDs)[27–29] and laser diodes (LDs),[30–36] has gained considerable interest in the OA field due to their low price, compact size, and high energy conversion efficiency.[37] LED-based systems are fundamentally limited by the low optical energy of individual LEDs when driven to generate ultrashort (nanosecond-duration) pulses, which necessitates the use of a very large number of LEDs to achieve sufficient per-pulse energies for deep-tissue imaging.[28,29,38,39] This, along with the high divergence of the output beam emitted by LEDs, significantly limits their contrast-to-noise-ratio (CNR) performance and effective imaging depth. LDs are considered more efficient sources due to their high optical energy. Individual pulsed LDs have been shown to provide up to ≈50 μJ when

X. Liu, I. Esteban, X. Chang, B. Zhang, X. L. Deán-Ben, D. Razansky
Institute for Biomedical Engineering
Department of Information Technology and Electrical Engineering
ETH Zurich
Zurich CH-8093, Switzerland
E-mail: daniel.razansky@uzh.ch

The ORCID identification number(s) for the author(s) of this article can be found under https://doi.org/10.1002/lpor.202501006

DOI: 10.1002/lpor.202501006

X. Liu, I. Esteban, X. Chang, B. Zhang, X. L. Deán-Ben, D. Razansky
Institute of Pharmacology and Toxicology and Institute for Biomedical Engineering
Faculty of Medicine
University of Zurich
Zurich CH-8057, Switzerland

F. Villani, A. Cossettini, L. Benini
Integrated Systems Laboratory
Department of Information Technology and Electrical Engineering
ETH Zurich
Zurich CH-8092, Switzerland
E-mail: lbenini@iis.ee.ethz.ch

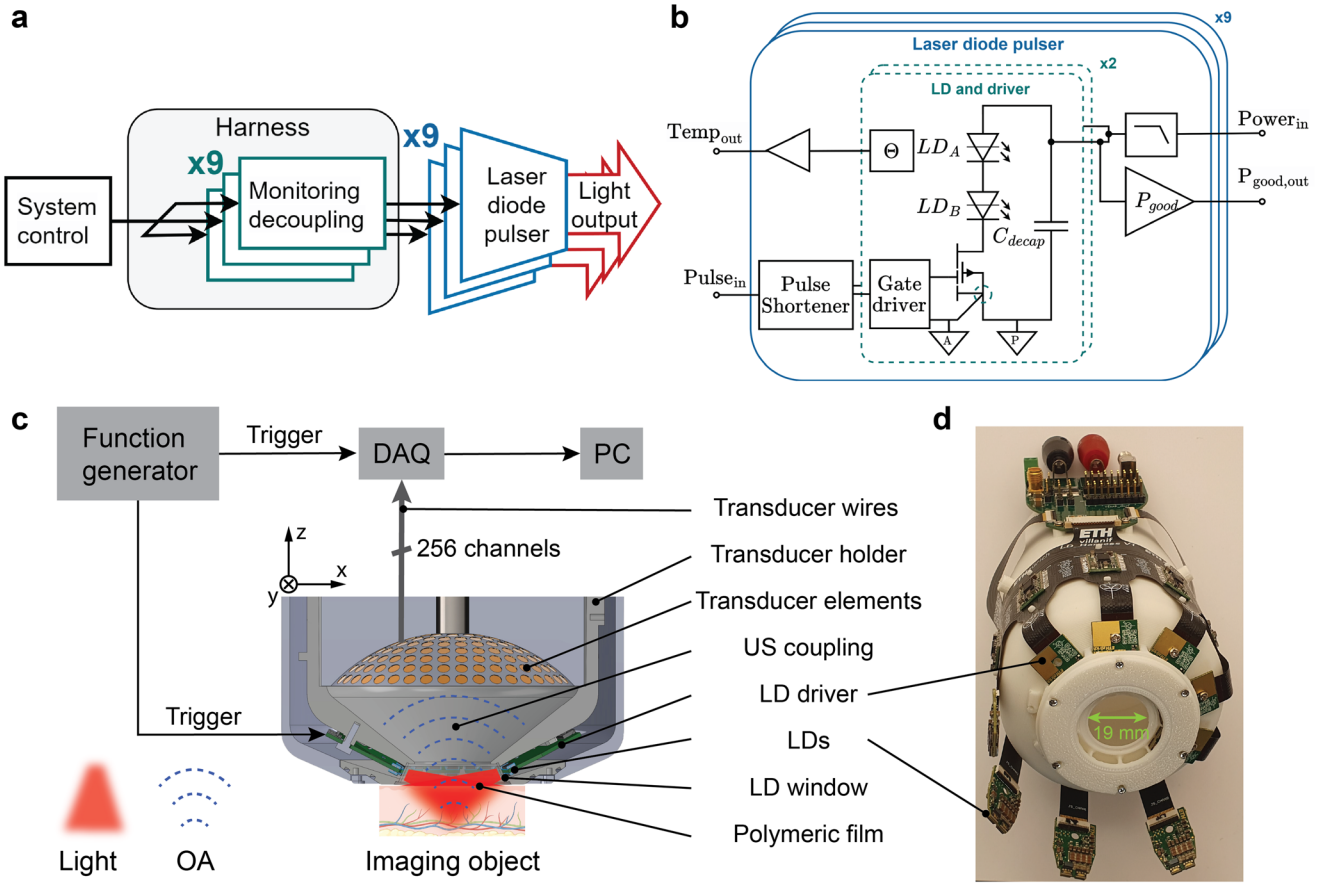

Figure 1. Schematics of the handheld embedded laser-diode illumination optoacoustic system (HELIOS). a) Overview of the LD light source. b) Block diagram of the LD pulser (LDP). c) Schematic representation of the main system components. DAQ – data acquisition system, PC – personal computer, LD – laser diode, OA – optoacoustic, US -ultrasound. d) Photograph of the actual system.

operated at 100 ns pulse width (PW). By stacking dozens of LDs, it is thus possible to achieve total per-pulse optical energy in the 2 mJ range.[37] To achieve a broader selection of wavelengths, OA signals can also be excited using intensity-modulated continuous wave (CW) LD sources, albeit at the expense of lower power.[40,41] Thereby, research efforts have focused on developing drivers capable of generating short pulses (10 s to 100 s of nanoseconds) by overdriving LDs with peak currents significantly exceeding those used for their normal CW operation.[42,43] These embodiments have been shown to produce sufficiently strong OA signals for practical applications in preclinical research.

Importantly, LDs are a particularly promising light source for facilitating the miniaturization of OA systems. While handheld systems based on linear array transducers integrating LDs[44–47] or SSLs[48,49] have been developed, such detection geometry is known to produce strong artifacts associated with limited tomographic view and out-of-plane illumination.[50,51] This commonly results in suboptimal image quality and diminished quantification abilities. Alternatively, real-time 3D image rendering with spherical array transducers is considered a preferrable OA imaging strategy, particularly when it comes to accurate visualization of vascular networks[52,53] and their clinically relevant alterations.[54] In this work, we devised a compact (83 mm diameter, 100 mm height, weight 840 g) and cost-effective handheld embedded laser-diode illumination optoacoustic system (HELIOS) based on a spherical array probe incorporating a compact LD-based illumination source located in close proximity to the imaged object. HELIOS is capable of rendering entire ≈1 cm^3 image volumes at 400 Hz frame rate and attains image quality on par with that obtained by OA systems using SSLs. We subsequently demonstrate volumetric angiography of human fingers and palm in a freehand mode with the system and perform large-scale volumetric compounding of vascular structures from the time-lapse 3D data. To showcase its dynamic imaging capabilities, we also captured finger vessel perfusion and pulsation of the radial artery.

2. Results

2.1. Compact HELIOS Design

HELIOS integrates a custom LD light source and a 256-element spherical array transducer into a compact and portable system (**Figure 1**). The LD light source consists of the system control module, the harness, nine monitoring and decoupling modules, and nine LD pulsers (LDPs) (Figure 1a). The LDP is a core component of the system, having a pulse shortener, gate driver, and GaN FET integrated onto a 6-layer printed circuit board (PCB) to

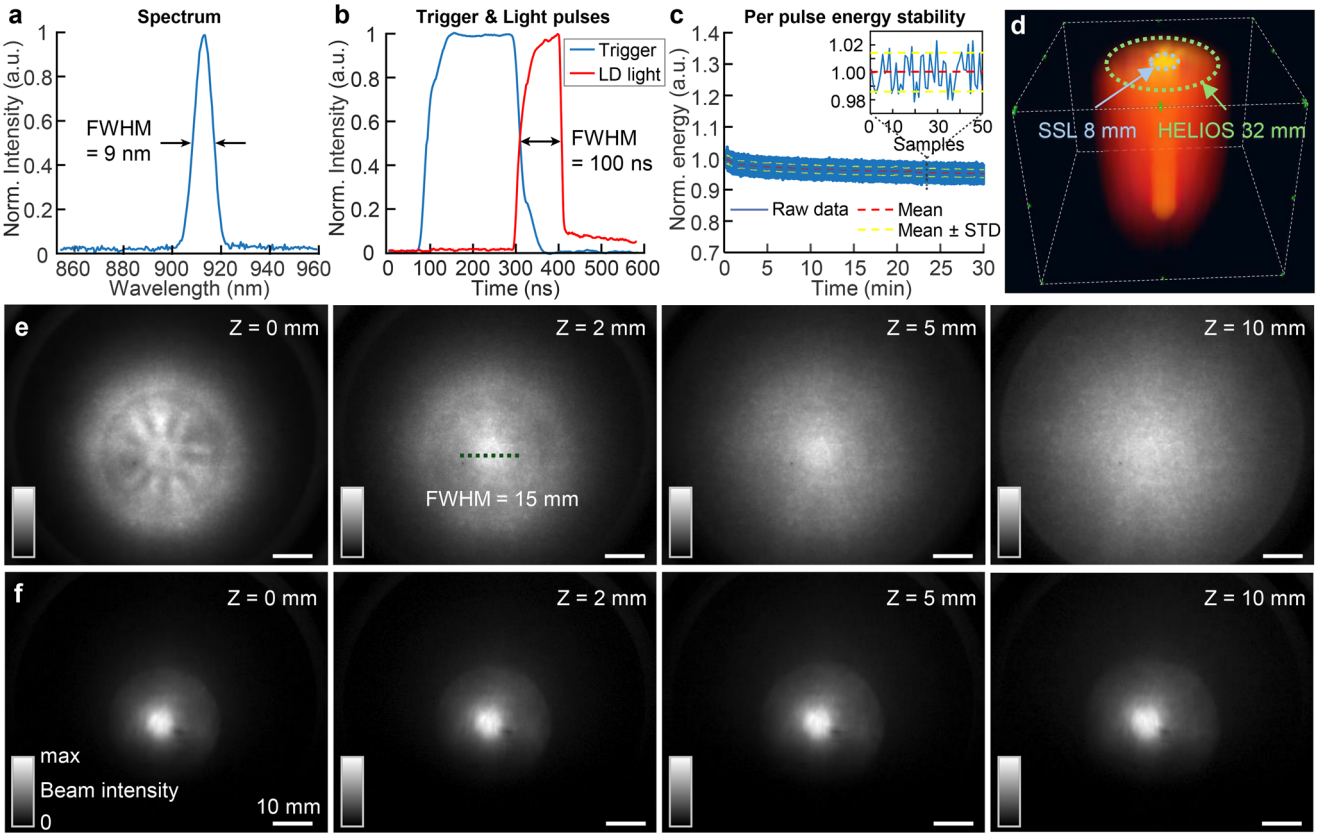

Figure 2. Characterization of HELIOS versus SSL-based illumination. a) Spectrum of the output beam emitted with HELIOS. b) Temporal profiles of the external trigger signal produced with a function generator and the emitted light pulse as measured with a photodiode. c) Per-pulse energy fluctuations for one million pulses measured over a period of ≈30 min. d) Rendered 3D illumination profiles of HELIOS and SSL, acquired on a sheet of paper with a CMOS camera for different distances along the light propagation (z) direction. e) 2D illumination profile of HELIOS for selected z positions. f) 2D illumination profile of SSL for selected z positions.

manage the timing and synchronization of LD pulses (Figure 1b, see Methods for details).

A schematic representation of the HELIOS system is shown in Figure 1c. A function generator enables synchronization of excitation and detection of OA responses by triggering the LDs and the data acquisition system (DAQ) simultaneously. The LDs emit light pulses with modulated PW set to 100 ns for optimal performance. The light beam emitted with each LD was directed toward the sample surface, thus facilitating the efficient generation of OA signals within the imaged region determined by the array's sensitivity field. Efficient OA wave transmission is ensured with a water coupling medium contained in a 3D-printed holder designed ad hoc to house the array and support the LD light source, including the LDs and their driving circuits (Figure 1d). This compact design enables versatile hand-held operation.

2.2. HELIOS Achieves Performance Comparable to SSL-based Systems

We first characterized the output beam of the LD light source. The emission optical spectrum exhibits a peak wavelength at 915 nm with a full width at half maximum (FWHM) of 9 nm (**Figure 2a**). To balance pulse energy and resolution, we applied a 200 ns external trigger that was shortened to a 100 ns light pulse by the pulse-shortening circuit (see Methods) for routine imaging (Figure 2b). The LD pulse energy stability was measured using a pyroelectric energy sensor at 500 Hz pulse repetition frequency (PRF). For this, a total of one million pulses were recorded over a period of ≈30 min. The standard deviation of the energy output over the entire acquisition period was only ±1.3%, indicating high pulse-to-pulse stability (Figure 2c). However, the mean energy exhibited a slight ≈2% decrease over time, most likely because the LD temperature rose from its cold-start value, reducing optical efficiency. This thermal effect highlights the need for effective heat management to maintain consistent optical output during extended operation. After reaching thermal equilibrium, per-pulse energy fluctuations stabilize within maximum and minimum bounds (inlet in Figure 2c).

We measured the 3D illumination profile of the HELIOS probe in air via z-stack acquisition with a CMOS camera (Figure 2d). The beam from the SSL, delivered from the centrally located fiber bundle, was collimated and therefore neither diverges nor scatters in air, forming an ≈8 mm-diameter cylindrical beam. In contrast, the LDs used in HELIOS illuminate the sample peripherally. The larger divergence angle (FWHM ≈25°) produces a

32 mm-diameter illumination area at the tissue surface, providing a more uniform light distribution across the imaged region of interest (ROI) as compared to the fiber-guided SSL source.

Figure 2e shows the beam profiles of HELIOS along the light propagation (z) direction in air. At z = 0 mm, closest to the LDPs, nine distinct beams from the peripheral LDPs are visible since each LD has a different divergence angle parallel and perpendicular to the *p*–*n* junction. At z = 2 mm the beams merge into a more uniform profile with an FWHM diameter of roughly 15 mm. Figure 2f presents the corresponding 2D beam profile of the SSL source; showing an approximately collimated beam retaining the same shape throughout the 0–10 mm z-range.

We benchmarked the HELIOS imaging performance against a conventional SSL source that delivers a higher per-pulse energy of 17 mJ but at a lower PRF of 100 Hz. Tissue-mimicking agar phantoms containing ≈100 µm diameter polyethylene microspheres (see Methods) were imaged to characterize spatial resolution. The HELIOS image is shown to exhibit more uniform contrast for most of the imaged spheres, effectively resulting in an increased FOV (**Figure 3**a,b). Sphere #1 appears with higher contrast in the SSL-based image because the laser provides top-down illumination, whereas HELIOS's annular beam delivers lower fluence at the center than at the periphery. The FWHM size of the reconstructed microspheres (273 µm, Figure 3c) corresponds to a spatial resolution of ≈250 µm, estimated as the root square difference of the measured FWHM and the particle diameter. When the excitation light pulses from SSL are delivered instead through the central aperture of the transducer array, the corresponding FWHM is 252 µm, which corresponds to a spatial resolution of 230 µm, as expected for this array.[55] HELIOS exhibits a resolution which is ≈20 µm inferior owning to the SSL's shorter PW (10 ns). The HELIOS curve was normalized to the peak amplitude of the SSL curve. The SSL profile exhibits a ≈2-fold higher OA intensity because of its stronger illumination.

Maximum-intensity projection (MIP) images along the y direction further highlight the superior contrast uniformity and the reduced depth-dependent fluence decay achieved with HELIOS (Figure 3d) compared with its SSL-based counterpart (Figure 3e). Figure 3f plots the OA signal intensity of each microsphere versus depth. Owing to HELIOS's broader illumination area, more spheres remain visible at depths of 5–6 mm than in the SSL-based images (see also Movie S1, Supporting Information). Figure 3f shows that the OA signal experiences less significant decay in the HELIOS image than in the SSL image. This is expected because the broader surface illumination of HELIOS reduces light attenuation with depth.[56]

The LD driving circuit ensures precise PW control, which is essential for balancing spatial resolution against PW. The LDs can deliver pulses from 10 up to 200 ns. Using a constant nominal 22 V driving voltage, we imaged human hair with PWs of 10, 20 ns, and then in 20 ns increments to a maximum of 200 ns. Pulse energy increased proportionally with PW (Note S1, Supporting Information). Figure 3g shows a representative image acquired with a 20 ns PW at a total pulse energy of 300 µJ. Due to the low pulse energy, the signals were averaged 100 times. Figure 3h shows that the minimum FWHM is 365 µm at 10 ns PW and increases gradually to 390 µm at 100 ns PW, remaining within the same resolution range. The hair sample lies outside the transducer's most sensitive zone, so its resolution is lower than that measured with microspheres. Once the PW exceeds 120 ns, however, resolution degrades rapidly because the stress-confinement condition is no longer satisfied per the given ultrasound (US) transducer's bandwidth. As Figure 3i shows, the OA intensity rises more than twenty-fold when the PW increases from 10 to 100 ns. Therefore, we selected a 100 ns PW as the best compromise between spatial resolution and signal strength.

To boost pulse energy, we over-drove the LD and imaged the hair phantom at driving voltages from 16 to 25 V with the 20 ns pulse. Although the OA intensity increased proportionally with pulse energy, the CNR did not scale accordingly, arguably because over-driving introduced streak artefact in the background. Spatial resolution likewise showed no meaningful improvement. We therefore adopted the nominal driving voltage of 22 V for routine operation (Note S1, Supporting Information).

2.3. Large-Scale Vascular Imaging in Healthy Volunteers

Experiments in healthy volunteers involved imaging of vascular networks in the fingers and palm to directly compare the HELIOS performance to SSL-based illumination in actual biological tissues. The HELIOS and SSL data were acquired in an alternate (interleaved) fashion during the same scan. The SSL beam was delivered via an optical fiber bundle inserted into the central aperture of the transducer, where the LD illumination was provided from the lateral sides of the spherical array transducer (Note S2, Supporting Information). The high PRF in this scheme ensures that the effectively imaged FOV with the two illumination sources is well aligned despite the movement of the imaging probe operated in a freehand mode.

To facilitate large-scale imaging in human subjects, the effective image volume acquired with each laser pulse can be significantly expanded by compounding (stitching) multiple time-lapse frames acquired in a hand-held mode[57] (**Figure 4**a-c). For this, the acquired frames were averaged 10 times, and a subset dataset was manually selected so that the probe displacement in consecutive frames constitutes 1–3 mm for optimal stitching performance (Note S3, Supporting Information). The algorithm detects rotation between consecutive frames in the Fourier domain, while the shifts are estimated from the associated phase changes. This provides the necessary rotation and translation parameters to reconstruct an image corresponding to a significantly enhanced FOV.

Figure 4d shows the imaging results of the middle finger dorsal side, obtained by a linear scan using the interleaved HELIOS and SSL illumination (Movie S2, Supporting Information). Consistent with the phantom results, the 3-D visualization through the fingernail-bed (Movie S3, Supporting information) demonstrates that the SSL-based system resolves superficial microvessels more clearly than HELIOS. To enable a more detailed comparison, we have added a zoomed-in view of the middle phalanx in Figure 4d. The effective FOV attained with HELIOS appears wider, which is ascribed to the broader illumination range achieved with LDs (Movie S4, Supporting information). Figure 4e presents an image of the palm acquired through a raster scan of the probe, with individual images subsequently stitched together (see Methods for details). To calculate the resulting im-

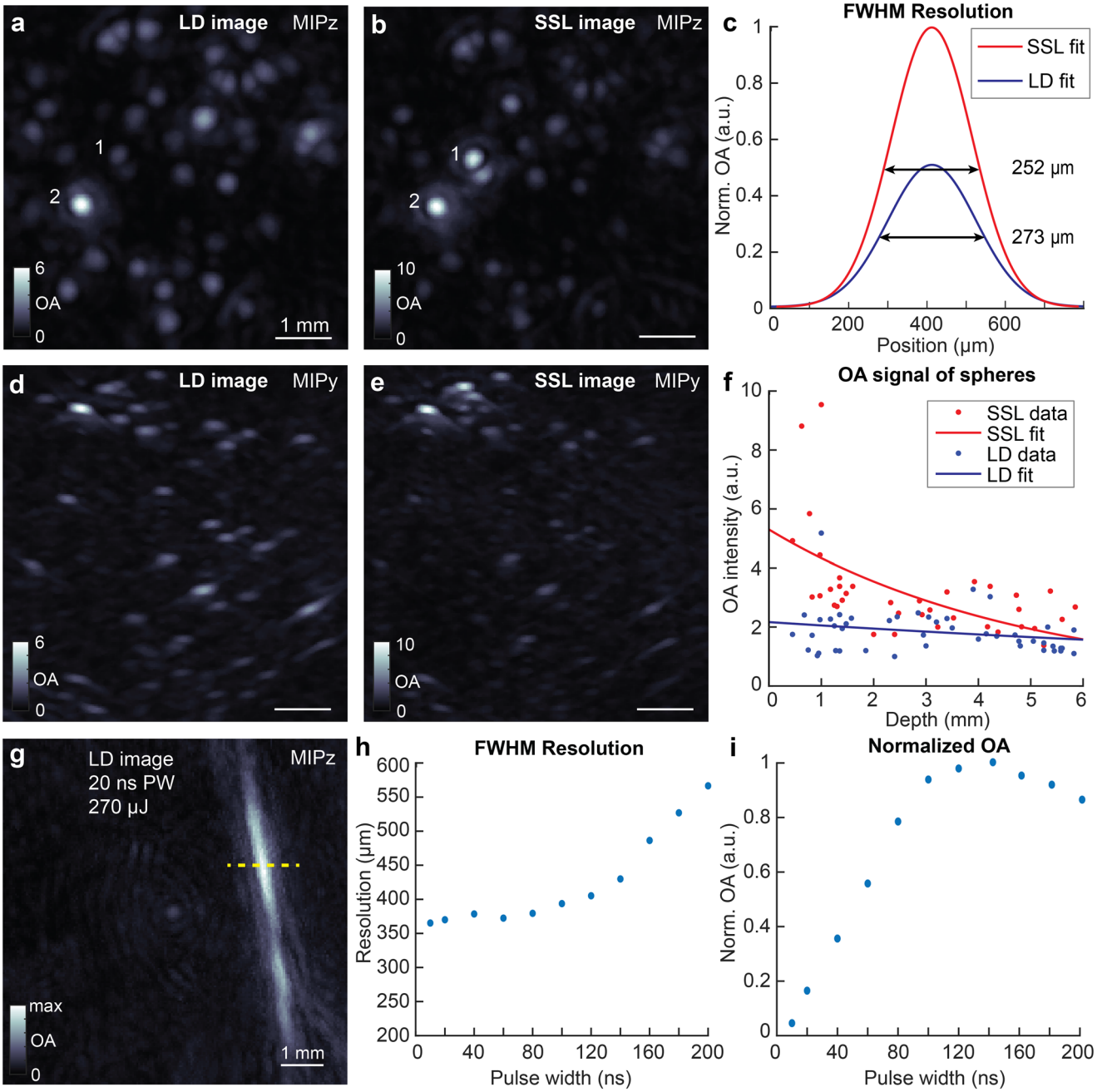

Figure 3. Performance of HELIOS versus SSL-based OA tomography. a) Images of an agar phantom with embedded 100 µm polyethylene microspheres. Maximum intensity projections (MIP) along z direction are shown. b) Corresponding MIP image taken with the SSL. c) Gaussian-fitted FWHM resolution profiles of the HELIOS and SSL. The HELIOS curve was normalized to the peak amplitude of the SSL curve. d) MIP along y direction of the HELIOS image. e) Corresponding MIP taken with the SSL. f) Comparison of the reconstructed OA signal intensity for microspheres located at different depths. g) MIP along z direction of a hair phantom image taken with the HELIOS system. h) Lateral resolution measured along the yellow dashed line in panel g as a function of pulsed width (PW). i) Normalized OA signal at the center of the dashed line as a function of PW.

age CNR, four pairs of ROIs and background regions were selected from each image. This yielded an average CNR of 31 dB for the HELIOS image, comparable to 34 dB for the SSL-based image of the palm. Note that the broader illumination profile of HELIOS results in larger reconstructed volumes with more vascular features covered by the images and more uniform contrast (fewer gaps).

2.4. Imaging Vascular Dynamics in Healthy Volunteers

The high-speed imaging capability of HELIOS is particularly beneficial for imaging biodynamics. To illustrate this, we conducted finger perfusion experiments in a healthy volunteer. A cuff was tightened around the finger to occlude the vessels, with the OA data acquisition commencing while the flow is blocked.

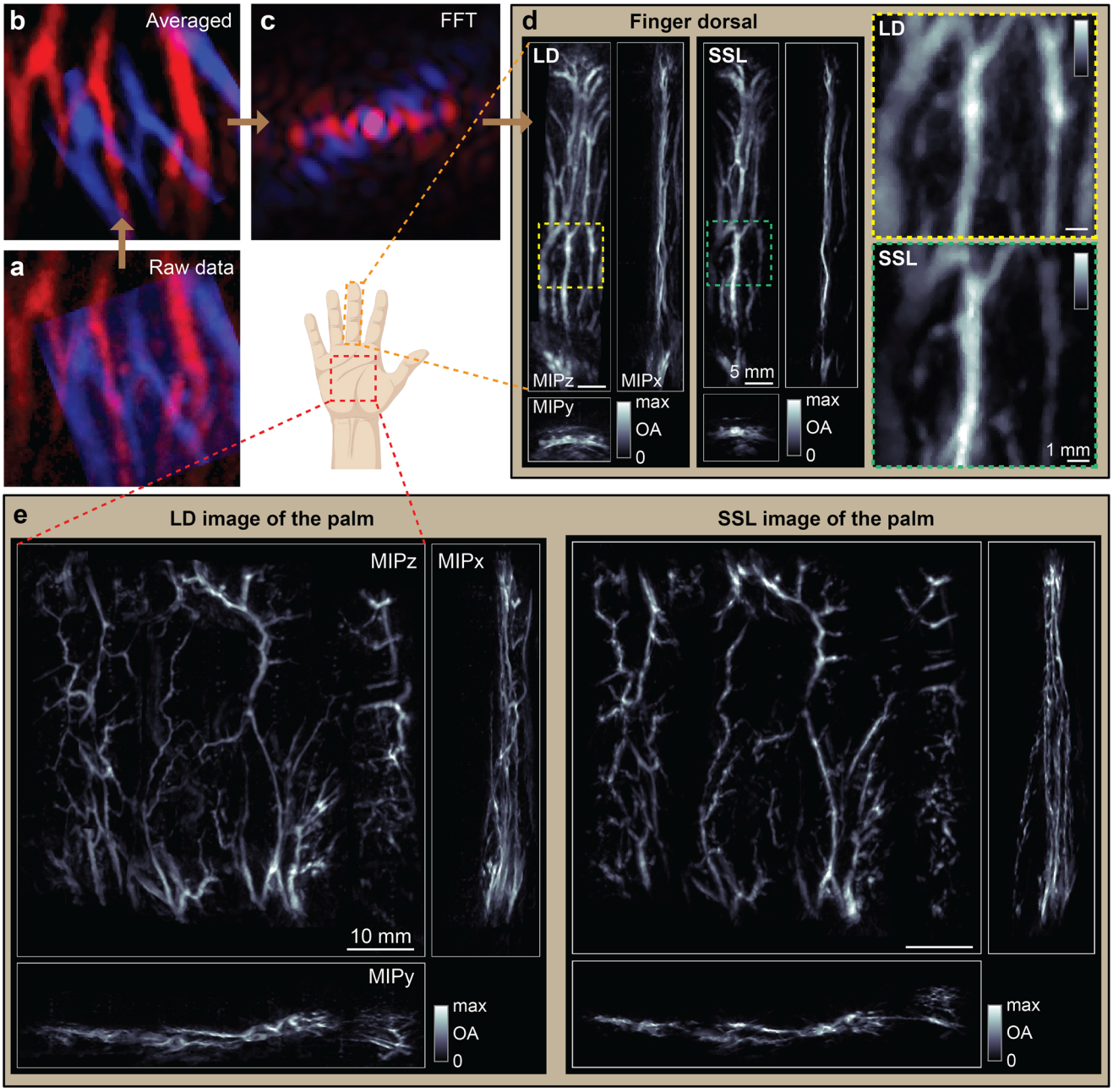

Figure 4. Imaging of fingers and palm in healthy volunteers. a) Overlay of two consecutive image volumes acquired by HELIOS without applying signal averaging. b) The two images after averaging 10 consecutive frames. c) Overlay of the Fourier transforms of the two images. d) Maximum intensity projections (MIPs) and zoomed-in view of the middle finger images acquired with HELIOS versus SSL. e) The corresponding palm.

At t = 0 s the cuff has been released, allowing the blood to reperfuse.

Figure 5a presents time-lapse OA images. By t≈2 s, dilation was observed in two deeply located vessels, while a superficial vessel gradually became visible. Figure 5b plots the normalized OA signal at a selected point on the superficial vessel (marked in panel a). The signal rises steeply after the release, confirming rapid reperfusion (Movie S6, Supporting information).

On the other hand, HELIOS was also shown to be capable of detecting arterial pulsation. Figure 5c presents a transverse cross-section of the wrist, the skin, two veins, and the radial artery. A zoomed-in view (Figure 5d) highlights the artery vessel wall motion due to pulsation. At t = 0 s the arterial wall is nearly flat, whereas at t = 0.2 s an incoming pulse causes it to bulge outward into a curved profile. Normalized OA signal at a selected location on the vessel wall reveals a clear arterial pulsation

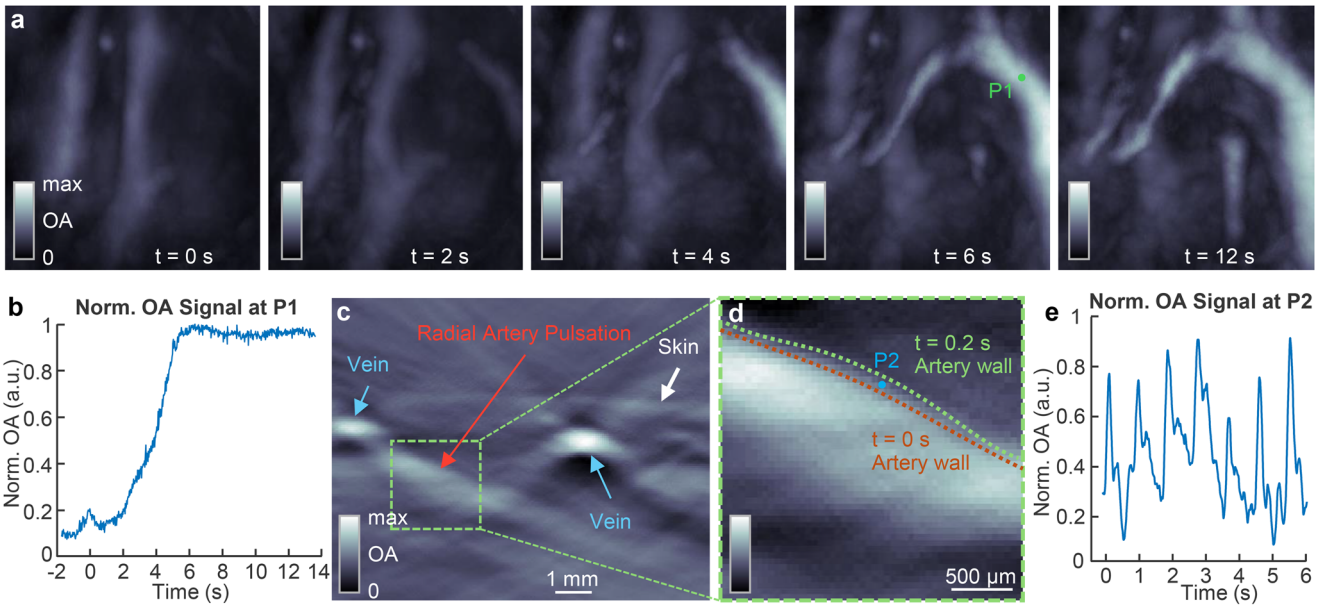

Figure 5. Dynamic imaging of finger vessel perfusion and radial artery pulsation. a) Time-lapse OA images of finger vessel reperfusion acquired with HELIOS. b) Normalized OA signal at the P1 location (labeled in panel a) as a function of time. c) OA wrist images acquired with HELIOS. d) Zoomed-in view highlighting radial-artery pulsation through changes in the vessel-wall shape. e) Normalized OA signal at the P2 location (labeled in panel d) showing the arterial pulsation rhythm.

rhythm (Figure 5e). The pulsation is best visualized in Movie S7 (Supporting Information).

3. Discussion

The presented results indicate that the developed compact HELIOS solution can render high quality OA images from deep tissues at a fraction of the cost as compared to conventional SSL-based systems. Specifically, the total cost of all the LD-based light sources and driving circuits is ~$5 k USD. The parallel acquisition and processing of the OA signals acquired with a 256-element spherical transducer array at a high frame rate of 400 Hz produced comparable results to those obtained with >$150 k SSL source, while offering substantial advantages in terms of portability and cost-effectiveness. The LD-based system is also effectively enhancing the FOV with respect to the previously reported SSL-based embodiments, mainly due to an optimized illumination strategy resulting in a broader and more uniform light distribution on the imaged tissue surface.

In the current implementation, the LD-based system employs a single-wavelength design for optimal energy delivery, which limits its ability to perform multispectral imaging compared to other tunable SSL-based OA systems.[58,59] Multi-wavelength illumination is possible with the existing design by replacing some of the 915 nm LDs with those operating at other wavelengths. Although the pulse energy for each wavelength is lower, it should be still sufficient for generating a detectable OA signal, as evinced by the hair experiment (Figure 3). However, lower per-pulse energy at each wavelength leads to a lower signal-to-noise ratio (SNR), which can potentially be overcome by increasing the number of averages, albeit to the detriment of real-time imaging performance. In fact, although the energy output (1.8 mJ) of the LD-based system is lower compared to that achieved with SSL (17 mJ), it was possible to achieve image quality comparable to SSL-based systems by averaging over 10 frames with the optimized illumination design, while maintaining a similar effective output frame rate. Acquisition of signals at a higher frame rate can also enable mitigating motion artifacts in multi-spectral imaging. The acquisition rate of the developed system is currently limited by the sampling speed of the electronics to a maximum of 400 Hz, considering 256 transducer elements, 256 samples acquired per channel per LD pulse, and 24 Msps sampling rate. In principle, acquisition at kHz frame rates is possible, but the per-pulse energy may need to be slightly reduced to conform to the laser exposure limits at near infrared wavelengths.[60] An additional constraint on achieving faster acquisitions is the maximal PRF of the LDs. To achieve a compact size of the handheld probe, no heat sink was integrated on the driving PCB, resulting in a maximal PRF of 500 Hz without causing overheating. Improved thermal management can potentially enable further PRF acceleration.

A low-cost angiographic volumetric OA imaging system has the potential to revolutionize medical diagnostics, particularly in resource-limited settings where access to advanced imaging technologies is limited. For example, it could aid in the early diagnosis of skin or breast cancer by visualizing blood vessel patterns and oxygen saturation levels in suspected lesions, parameters not accessible with pulse-echo US imaging.[61,62] It may further facilitate better wound care and management of diabetic foot ulcers by providing insights into tissue perfusion to prevent unnecessary complications. The affordability and portability of the LD-based system make it particularly well-suited for point-of-care applications in remote or underserved areas, facilitating timely diagnoses and improving patient outcomes. Clinical OA systems are commonly equipped with dual-mode cross-sectional OA/US imaging capabilities.[63,64] The current HELIOS implementation

could be readily upgraded for the dual-mode operation, although this would inevitably result in reduced imaging frame rates given the limitations of the currently available acquisition hardware.[65] Combined volumetric OA and cross-sectional US imaging has also been implemented using a multi-segment spherical array incorporating a linear array segment for B-mode imaging, [53] which can potentially be integrated into the next generation HELIOS.

In conclusion, HELIOS represents a significant leap toward accessible, affordable, and practical OA imaging solutions for clinical and point-of-care applications. By demonstrating high-resolution, high-speed imaging capabilities comparable to traditional SSL-based systems at a fraction of the cost, the proposed solution challenges the notion that superior OA image quality requires expensive and bulky illumination sources, which opens new possibilities for bedside diagnostics. As OA imaging continues to evolve, this innovation paves the way for its broader adoption in clinical practice, ultimately bringing the benefits of this modality to a wider patient population.

4. Experimental Section

Ultrasound Transducer Array: OA signals were collected with a spherical matrix transducer array (Imasonic SaS, Voray, France) consisting of 256 piezocomposite ultrasonic elements arranged on a spherical surface spanning a 90° angle.[55] Each ultrasonic element measures $\approx 3 \times 3$ mm^2, with its normal vector precisely aligned toward the center of the spherical geometry. This configuration ensures optimal sensitivity and uniform signal detection across all elements within the ROI centered around the sphere's focal point. The transducer elements exhibit a central frequency of 4 MHz with a FWHM bandwidth of 100%, allowing for a broad frequency response and high-resolution imaging.

Notably, the cylindrical body of the transducer features a central aperture designed to accommodate an optical fiber. This aperture allows the integration of a tunable SSL source for illumination, enabling a direct comparison with LD-based imaging.

Laser Diode Driver System: HELIOS incorporates multiple LDs arranged in a modular, hierarchical architecture. Its main component is the 915 nm LD module (OSRAM SMT Laser, SPL S4L90A_3 A01). Four such modules are mounted on a single LDP, with each module receiving power through a locally decoupled power supply. The LDP is externally triggered to generate synchronized light pulses from all LDs.

Nine LDPs were connected via a single flexible PCB harness that integrates nine dedicated monitoring and decoupling modules (one per LDP). These modules manage power domain isolation, monitor power consumption, and facilitate pulse synchronization. A central control PCB supplies power and trigger signals to all LDPs and provides real-time monitoring of current draw, board temperature, and LD voltage on a per-LDP basis.

In total, the assembly drives 36 LD modules in synchrony. Each LD module delivers a peak optical power of 500 W, resulting in a combined peak optical power of 18 kW and a peak power consumption of 63 kW. The system is designed to generate LD pulses ranging from 10 to 200 ns, yielding a pulse energy of 1.8 mJ for a typical 100 ns pulse. The following sections detail the design strategies and technical solutions that enable this performance (Note S4, Supporting Information).

Each LD module is operated at 11 V and 160 A, with the 36 modules combined producing a peak current of 5.8 kA. Generating synchronized, nanosecond-scale pulses at 5.8 kA in a compact, handheld module with minimal electromagnetic interference (EMI) presents a substantial engineering challenge. To supply the high current required, two LD modules are connected in series, with each group of two modules driven by a low-side GaN FET (EPC2619, EPC Corporation). Compared to traditional MOSFETs, GaN FETs offer lower switching energy and faster switching speeds.[66]

To ensure efficient power delivery, the supply circuits are designed with low impedance in the pulsing frequency range—dictated by the rising edge and PW—by minimizing trace length and maximizing trace width. The transmission pulse is decoupled into different frequency components by three banks of decoupling capacitors: 1) Rising edge frequency component consisting of 30 capacitors (47 nF, low equivalent series inductance, TDK) to decouple the ≈10 ns rising edge; 2) pulse duration frequency component consisting of 20 capacitors (2.2 µF, Murata) to decouple the pulse duration (10–200 ns); 3) bulk capacitance consisting of 10 capacitors (10 µF, Murata) to provide bulk capacitance and serve as the first stage of the input low-pass filter.

A two-stage pi low-pass filter isolates the decoupling capacitor network from the rest of the system, providing >120 dB attenuation between 150 kHz and 280 MHz. This filter prevents high-frequency noise from propagating from the LDs and reduces the instantaneous current drawn from the power supply.

The pulser circuitry is implemented on a 1 mm thick, 6-layer PCB. The four internal copper planes are constructed with 70 µm thick copper, and blind vias are copper filled to enhance current conduction and thermal dissipation.

The pulsing control section of the LDP depicted in Figure 1b (pulse shortener, gate driver, and GaN FET) manages the timing and synchronization of LD pulses. The star ground for the system is formed by the gates of the two GaN FETs. The module operates with two distinct power domains, namely, the 22 V high-power rail that drives the LDs and the low-power signal rail that provides pulser control.

Each GaN FET is driven by a GaN FET driver circuit (LMG1020, Texas Instruments, USA). To minimize EMI on the low-power rail, each LMG1020 driver is individually decoupled. Both drivers are controlled by an AND gate configured with a resistor–capacitor circuit for pulse shortening. This configuration allows the use of signal generators even when their minimal PW is limited. Each module connects to the rest of the system via a Flexible Printed Circuit connector designed to supply up to 3 A of peak current to the pulser.

The LDP module interfaces with the overall system through a flexible PCB harness, as shown in Figure 1d. The harness is designed to connect all LD pulsers to the power supply, align the front-end laser pulsers mechanically, and also serves as the base for individual LDP control and decoupling modules.

Each LDP is decoupled via a dedicated monitoring and decoupling module. This decoupling prevents ground loops caused by direct connections between power and signal domains at the harness level. Ground loops could arise from the power domain → signal domain → power domain pathways in another LDP. Since each module generates a significant amount of energy in a very short time (320 A at 22 V for 10 to 200 ns), and because the pulser module surrounds the US transducer, even minor ground loops could generate substantial EMI, impacting US acquisition.

To mitigate these issues, the signal power domain is not galvanically isolated as this would lead to excessive power drawing. Instead, it is decoupled using a pi filter that functions as both a common-mode and differential filter in the 10 to 100 MHz pulse frequency range. A digital isolator (MAX22291C, Analog Devices, USA) transmits the pulser control signal over the common mode choke and drives a delay-settable gate that adjusts delays for precise pulse synchronization across all LDPs. Additionally, this module monitors each LDP's current draw using a high-side current monitor (INA139NA, Texas Instruments).

The entire system is controlled and monitored through an interface PCB that provides access to real-time monitoring of pulse duration, current consumption, and board temperature for each LDP, thereby enabling fault detection during operation.

Handheld System Design: A holder was designed ad hoc and 3D-printed to integrate all components into a compact and handheld system, achieving both portability and optimal performance. The holder consists of several key components, each designed to ensure precise alignment, effective functionality, and reliability. At the core of the system is the transducer holder, which securely houses the spherical transducer using a rub-

ber O-ring placed between the transducer and the holder. This design not only stabilizes the transducer but also ensures that the center of the transducer's spherical geometry lies 4 mm below the surface of the imaging target, which is aimed at optimizing imaging depth for better signal detection and deeper tissue visualization.

Nine LDP were evenly distributed in a circular arrangement, each angled downward at 23° toward the spherical center. The LDs, featuring a FWHM beam divergence of 25° vertically, were placed on a 24 mm-diameter circle. This compact arrangement minimizes energy loss due to beam divergence and ensures high photon energy density at the target area, significantly enhancing OA signal generation. The generated OA waves propagate through the thin polymeric film and the encapsulated water coupling medium to the transducer surface. To maximize optical fluence, the LDs were positioned as close as possible to the imaged ROI. Additionally, an aperture size of 19 mm was maintained to ensure unobstructed OA wave transmission.

The flexible PCB harness was wrapped around the exterior of the transducer array holder to connect all the 9 LDPs. The system incorporated multiple sealing components to prevent leakage of the water medium between the polymeric film and the array surface. A transparent polymethyl methacrylate (PMMA) ring, CNC-machined from a single PMMA cube and meticulously polished to enhance light transmission and minimize refraction or diffusion, served as a critical component of the LD optical window. It facilitates the coupling of light from the LDs while safeguarding the internal components from water intrusion. Compared to a multielement transparent window, the single piece full ring window increased the light transparency and sealing effectiveness. Another 3D-printed flange ring tightly secured the thin polymeric film and incorporated rubber O-rings to prevent leakage of coupling water from the transducer and block external water or US gel from entering the sensitive internal electronics (Note S5, Supporting Information).

The outermost layer of the design included a protective cover that not only safeguarded the internal electronics but also provided ergonomic support for handheld use. With a simple design modification, this cover was adapted to mount the probe on a stage for precise raster-scanning operations, enabling high-resolution imaging across larger areas and facilitating improved image stitching. The integration of components into a compact form factor ensures the system achieves optimal laser energy delivery, maximizes OA signal detection, and enhances imaging depth, all while maintaining reliability and ease of use.

Data Acquisition: Data acquisition was performed in two modes: LD-only or LD-SSL-combined. An OPO SSL (EVO II, Innolas Laser GmbH, Krailling, Germany) guided though a fiber bundle inserted in the central aperture of the US transducer was used as the excitation source in the combined LD-SSL configuration. The measured pulse energy at the output of the bundle was ≈17 mJ at 100 Hz PRF, while the total per pulse optical energy of the LD system was 1.8 mJ.

In the LD-only mode, OA signals from all 256 channels were simultaneously sampled at 24 Msps, with 256 samples collected per signal. This enabled the system to achieve a frame rate of 400 Hz. In the combined LD-SSL mode, the SSL served as the trigger source at 100 Hz for a function generator (FG1) generating a 3-cycle square signal at 300 Hz, i.e., FG1 introduces a 2.5 ms delay and generates three triggers at intervals of 2.5 ms. A second function generator (FG2) was used to shorten the trigger signals to 200 ns needed to drive the LD drivers. With this configuration, 3 LD pulses were interleaved between each SSL pulse. The 100 Hz SSL trigger and the 300 Hz LD trigger were simultaneously input into the DAQ system, practically resulting in acquisition of OA signals at 400 frames per second (Note S1, Supporting Information). This dual-mode acquisition allows a direct comparison between images simultaneously acquired by both LD and SSL systems from the same object.

Data Processing and Reconstruction: The collected data was first divided into two separate datasets corresponding to SSL and LD excitation, respectively. The LD data were averaged over 10 frames, resulting in a 3.2-fold improvement in SNR. As a result, the frame rate decreased from 300 to 30 Hz. Further increasing the signal averaging does not substantially improve the CNR (Note S6, Supporting Information). To ensure a comparable frame rate for analysis, the SSL data were averaged over 3 frames, resulting in a 33 Hz frame rate and a 1.7-fold improvement in SNR.

Both the SSL and LD pulsed currents introduced EMI, which coupled uniformly across all 256 piezoelectric elements of the transducer array in each channel. To eliminate this interference without affecting the actual OA signal, the mean signal across all 256 channels at each time point was subtracted from each individual channel. Finally, the processed data was reconstructed into 10 mm^3 3D image volumes using a graphics processing unit (GPU)-based back-projection algorithm.[67]

Volumetric Image Compounding (Stitching): To achieve a larger FOV, the reconstructed time-lapse 3D volumetric datasets acquired in a free-hand motion mode were compounded into a larger dataset using a Fourier-based algorithm.[57] This algorithm leverages frequency-domain properties of vascular networks in OA images to estimate the relative motion and orientation of the imaging probe. This enables the rapid combination of sequential volumetric frames into large-area scans without the need for additional tracking hardware. To ensure accurate compounding results, the same vascular structures must be visible in consecutive frames, while excessive spatial overlap may also lead to cumulative errors and blurring of vascular structures in the compounded image. Therefore, the data acquisition was optimized by controlling the probe's movement speed and removing redundant frames during image processing.

Phantoms: Polyethylene microspheres (100 µm diameter, Cospheric Inc, USA) were embedded in 1.3% (by weight) agar to create a phantom for testing the system's resolution. To simulate the optical scattering properties of biological tissues, 1.2% (by volume) Intralipid was added to the agar, resulting in a reduced scattering coefficient of $\mu_s' = 10\ cm^{-1}$. Ink was incorporated to mimic the optical absorption of tissues, providing an absorption coefficient of $\mu_a = 0.23\ cm^{-1}$. The microspheres were uniformly distributed throughout the agar phantom.

Vascular Imaging in Healthy Volunteers: Vascular networks in the fingers and the palm of healthy volunteers were imaged to demonstrate the system's performance in real handheld clinical imaging scenarios. The probe was first linearly scanned in a handheld fashion along a middle finger. For imaging the palm, an XY stage (IAI Corporation, Japan) was used instead to hold the probe and perform a raster scan of a larger area while avoiding gaps between the scan tracks. The stage was moved continuously along the *X*-axis for 50 mm, followed by a 7 mm step along the *Y*-axis to the next line, then reversed direction along the *X*-axis for another 50 mm. This process was repeated for a total of 7 steps along the *Y*-axis, resulting in a 50 × 50 mm compounded FOV.

Supporting Information

Supporting Information is available from the Wiley Online Library or from the author.

Acknowledgements

X.L. and F.V. contributed equally to this work. The authors would like to thank D. Nozdriukhin, C. Özsoy, and L. Tang for their assistance with the experiments. Funding: This work was supported by the ETH Research Grant ETH-C-01-21-2 (Project ListenToLight).

Conflict of Interest

The authors declare no conflict of interest.

Author Contributions

X.L. and F.V. contributed equally to this paper. X. L.: Conceptualization, Methodology, Investigation, Experimentation, Data curation, Software, Formal analysis, Visualization, Writing – original draft, Writing – review

& editing. F. V.: PCB system design, Methodology, Investigation, Writing – original draft, Writing – review & editing. I. E. V.: Data curation, Software. X. C. & B. Z.: Investigation, Experimentation. A. C.: Investigation, Writing – review & editing. X. L. D. B.: Software, Resources, Formal analysis, Writing – review & editing. L. B.: Project administration, Resources, Supervision, Writing – review & editing. D. R.: Conceptualization, Methodology, Project administration, Resources, Supervision, Validation, Writing – review & editing.

Data Availability Statement

The electronics design files of the main system modules are available at a github repository https://github.com/pulp-bio/HELIOS-R. Other data supporting the findings of this study are available from the corresponding author upon reasonable request.

Keywords

Optoacoustic Tomography, Photoacoustic, Compact, Handheld, Low cost, Nir wavelength, Laser diode, Vasculature

Received: April 27, 2025
Revised: June 29, 2025
Published online: July 28, 2025

[1] M. H. Xu, L. H. V. Wang, *Rev. Sci. Instrum.* **2006**, *77*, 041101.
[2] P. Beard, *Interface Focus* **2011**, *1*, 602.
[3] S. J. Ford, P. L. Bigliardi, T. C. P. Sardella, A. Urich, N. C. Burton, M. Kacprowicz, M. Bigliardi, M. Olivo, D. Razansky, *J. Invest. Dermatol.* **2016**, *136*, 753.
[4] W. Zhang, H. Ma, Z. Cheng, Z. Wang, L. Zhang, S. Yang, *Quant Imaging Med. Surg.* **2019**, *9*, 807.
[5] J. Ahn, J. Y. Kim, W. Choi, C. Kim, *Photoacoustics* **2021**, *23*, 100282.
[6] L. Lin, P. Hu, X. Tong, S. Na, R. Cao, X. Y. Yuan, D. C. Garrett, J. H. Shi, K. Maslov, L. H. V. Wang, *Nat. Commun.* **2021**, *12*, 882.
[7] Ç. Özsoy, A. Özbek, M. Reiss, X. L. Deán-Ben, D. Razansky, *P. N. A. S.* **2021**, *118*, 2103979118.
[8] S. Wilkinson, J. Cummings, S. Zafar, M. Kozar, J. Manning, G. Dinsdale, M. Berks, C. Taylor, M. Dickinson, A. L. Herrick, A. K. Murray, *Sci. Rep.* **2022**, *12*, 20446.
[9] K. Jansen, G. van Soest, A. F. W. van der Steen, *Ultrasound in Medicine and Biology* **2014**, *40*, 1037.
[10] S. Iskander-Rizk, A. F. W. van der Steen, G. van Soest, *Physics in Medicine and Biology* **2019**, *64*, 16TR01.
[11] I. Ivankovic, E. Mercep, C.-G. Schmedt, X. L. Deán-Ben, D. Razansky, *Radiology* **2019**, *291*, 45.
[12] A. Karlas, M. Bariotakis, M. Kallmayer, L. Hadjileontiadis, M. Wildgruber, *Frontiers in Cardiovascular Medicine* **2023**, *10*, 1178101.
[13] M. E. Karakatsani, D. Nozdriukhin, S. Tiemann, H. A. I. Yoshihara, R. Storz, M. Belau, R. Ni, D. Razansky, X. L. Deán-Ben, *Alzheimers Dement.* **2025**, *21*, 14511.
[14] R. Ni, Z. Chen, X. L. Deán-Ben, F. F. Voigt, D. Kirschenbaum, G. Shi, A. Villois, Q. Zhou, A. Crimi, P. Arosio, R. M. Nitsch, K. P. R. Nilsson, A. Aguzzi, F. Helmchen, J. Klohs, D. Razansky, *Nat. Biomed. Eng.* **2022**, *6*, 1031.
[15] L. R. McNally, M. Mezera, D. E. Morgan, P. J. Frederick, E. S. Yang, I.-E. Eltoum, W. E. Grizzle, *Clin. Cancer Res.* **2016**, *22*, 3432.
[16] N. Nyayapathi, J. Xia, *J. Biomed. Opt.* **2019**, *24*, 121911.
[17] A. Ron, X. L. Deán-Ben, S. Gottschalk, D. Razansky, *Cancer Res.* **2019**, *79*, 4767.
[18] X. L. Deán-Ben, I. Weidenfeld, O. Degtyaruk, V. Ntziachristos, A. C. Stiel, D. Razansky, *Neoplasia* **2020**, *22*, 441.
[19] C. Liu, J. Chen, Y. Zhang, J. Zhu, L. Wang, *Advanced Photonics* **2021**, *3*, 016002.
[20] J. W. Baik, H. Kim, M. Son, J. Choi, K. G. Kim, J. H. Baek, Y. H. Park, J. An, H. Y. Choi, S. Y. Ryu, J. Y. Kim, K. Byun, C. Kim, *Laser Photonics Rev.* **2021**, *15*, 2100124.
[21] W. Y. Li, Y. H. Liu, F. Kubo, S. Werner, D. Razansky, *Commun. Biol.* **2024**, *7*, 1574.
[22] Y. Ying, H. Zhang, L. Lin, *Optics* **2024**, *5*, 133.
[23] J. Jo, C. Tian, G. Xu, J. Sarazin, E. Schiopu, G. Gandikota, X. Wang, *Photoacoustics* **2018**, *12*, 82.
[24] A. P. Regensburger, L. M. Fonteyne, J. Jüngert, A. L. Wagner, T. Gerhalter, A. M. Nagel, R. Heiss, F. Flenkenthaler, M. Qurashi, M. F. Neurath, N. Klymiuk, E. Kemter, T. Fröhlich, M. Uder, J. Woelfle, W. Rascher, R. Trollmann, E. Wolf, M. J. Waldner, F. Knieling, *Nat. Med.* **2019**, *25*, 1905.
[25] J. Park, S. Choi, F. Knieling, B. Clingman, S. Bohndiek, L. V. Wang, C. Kim, *Nature Reviews Bioengineering* **2024**, *3*, 193.
[26] J. J. M. Riksen, A. V. Nikolaev, G. van Soest, *J. Biomed. Opt.* **2023**, *28*, 121205.
[27] T. J. Allen, P. C. Beard, *Biomed. Opt. Express* **2016**, *7*, 1260.
[28] W. Xia, M. Kuniyil Ajith Singh, E. Maneas, N. Sato, Y. Shigeta, T. Agano, S. Ourselin, S. J. West, A. E. Desjardins, *Sensors* **2018**, *18*, 1394.
[29] X. Liu, S. K. Kalva, B. Lafci, D. Nozdriukhin, X. L. Dean-Ben, D. Razansky, *Photoacoustics* **2023**, *31*, 100521.
[30] A. Hariri, A. Fatima, N. Mohammadian, S. Mahmoodkalayeh, M. A. Ansari, N. Bely, M. R. N. Avanaki, *J. Biomed. Opt.* **2017**, *22*, 075001.
[31] Ç. Özsoy, A. Cossettini, A. Özbek, S. Vostrikov, P. Hager, X. L. Deán-Ben, *Ieee Transactions on Medical Imaging* **2021**, *40*, 2023.
[32] A. W. Sari, R. Widyaningrum, A. Setiawan, Mitrayana, *Appl. Acoust.* **2024**, *218*, 109903.
[33] S. Khan, S. Mukhopadhyay, S. Vasudevan, G. Goel, D. Joshi, N. Kapoor, S. Das, *J. Biomed. Opt.* **2024**, *29*, 017002.
[34] H. Zhong, J. Zhang, T. Duan, H. Lan, M. Zhou, F. Gao, *Opt. Lett.* **2019**, *44*, 1988.
[35] S. K. Kalva, P. K. Upputuri, M. Pramanik, *Opt. Lett.* **2019**, *44*, 81.
[36] B. X. Huang, S. C. K. Chan, X. Li, V. T. C. Tsang, T. T. W. Wong, *Laser Photonics Rev.* **2024**, *18*, 2400452.
[37] M. K. A. Singh, W. F. Xia, *Sensors* **2020**, *20*, 6173.
[38] Y. H. Zhu, G. Xu, J. Yuan, J. G. Jo, G. Gandikota, H. Demirci, T. Agano, N. Sato, Y. Shigeta, X. D. Wang, *Sci. Rep.* **2018**, *8*, 9885.
[39] Y. Zhu, T. Feng, Q. Cheng, X. Wang, S. Du, N. Sato, J. Yuan, M. Kuniyil Ajith Singh, *Sensors* **2020**, *20*, 2484.
[40] A. Stylogiannis, L. Prade, A. Buehler, J. Aguirre, G. Sergiadis, V. Ntziachristos, *Photoacoustics* **2018**, *9*, 31.
[41] P. Kalitsounakis, G. Zacharakis, G. J. Tserevelakis, *J. Microsc.* **2025**, *298*, 3.
[42] M. Seeger, A. Stylogiannis, L. Prade, S. Glasl, V. Ntziachristos, *Sci. Rep.* **2023**, *13*, 19542.
[43] X. Liu, W. Li, Y.u-H. Liu, H. Estrada, D. Razansky, *Opt. Lett.* **2024**, *49*, 6865.
[44] P. J. van den Berg, K. Daoudi, H. J. Bernelot Moens, W. Steenbergen, *Photoacoustics* **2017**, *8*, 8.
[45] C. Canal, A. Laugustin, A. Kohl, O. Rabot, *SPIE* **2016**, *9887*, 230.
[46] K. Daoudi, P. J. van den Berg, O. Rabot, A. Kohl, S. Tisserand, P. Brands, W. Steenbergen, *Opt. Express* **2014**, *22*, 26365.
[47] M. Mitra, A. Haworth, P. Gaddale, F. Badran, N. Lagno, C. Pameijer, F. Aziz, S.-R. Kothapalli, *Journal of Biophotonics* **2024**, *17*, 202400058.
[48] C. Lee, S. Cho, D. Lee, J. Lee, J.-I. Park, H.-J. Kim, S. H. Park, W. Choi, U. Kim, C. Kim, *Photoacoustics* **2023**, *31*, 100512
[49] D. H. Jiang, Hongbo Chen, Rui Zheng, Fei Gao, *J. Appl. Phys.* **2022**, *132*, 074904.

[50] H. N. Y. Nguyen, W. Steenbergen, *Photoacoustics* **2020**, *19*, 100176.
[51] W. C. Vogt, C. Jia, K. A. Wear, B. S. Garra, T. J. Pfefer, *Frontiers in Optics 2017*, Optica Publishing Group, Washington, D.C. **2017**.
[52] X. L. Deán-Ben, A. Ozbek, D. Razansky, *Ieee Transactions on Medical Imaging* **2013**, *32*, 2050.
[53] H.-C. A. Lin, X. L. Deán-Ben, A. Ozbek, Y.-H. Shao, B. Lafci, D. Razansky, *Opt. Lett.* **2024**, *49*, 1469.
[54] Y. Matsumoto, Y. Asao, A. Yoshikawa, H. Sekiguchi, M. Takada, M. Furu, S. Saito, M. Kataoka, H. Abe, T. Yagi, K. Togashi, M. Toi, *Sci. Rep.* **2018**, *8*, 786.
[55] X. L. Dean-Ben, D. Razansky, *Opt. Express* **2013**, *21*, 28062.
[56] S. K. Kalva, X. L. Dean-Ben, D. Razansky, *Photonics Res.* **2021**, *9*, 899.
[57] N. Knauer, X. L. Dean-Ben, D. Razansky, *IEEE Trans. Med. Imaging* **2020**, *39*, 1160.
[58] J. Kim, B. Park, J. Ha, I. Steinberg, S. M. Hooper, C. Jeong, E.-Y. Park, W. Choi, T. Liang, J.a S. Bae, R. Managuli, Y. Kim, S. S. Gambhir, D.-J. Lim, C. Kim, *Cancer Res.* **2021**, *81*, 4849.
[59] I. Ivankovic, H.-C. Amy Lin, A. Özbek, A. Orive, X. L. Deán-Ben, D. Razansky, *Adv. Sci.* **2024**, *11*, 2470106.
[60] I. C. N.-I. Radiat, *Health Phys.* **2013**, *105*, 271.
[61] X. L. Deán-Ben, D. Razansky, *Experimental Dermatology* **2021**, *30*, 1598.
[62] L. Lin, P. Hu, J. H. Shi, C. M. Appleton, K. Maslov, L. Li, R. Y. Zhang, L. H. V. Zhang, *Nat. Commun.* **2018**, *9*, 2352.
[63] J. Kim, S. Park, Y. Jung, S. Chang, J. Park, Y. Zhang, J. F. Lovell, C. Kim, *Sci. Rep.* **2016**, *6*, 35137.
[64] Y. T. Wen, D. Guo, J. Zhang, X. Liu, T. Liu, L. Liu, S. Jiang, D. Wu, H. Jiang, *Frontiers in Physiology* **2022**, *13*, 1036621.
[65] D. Nozdriukhin, S. K. Kalva, C. Özsoy, M. Reiss, W. Li, D. Razansky, X. L. Deán-Ben, *Adv. Sci.* **2024**, *11*, 2306087.
[66] K. J. Chen, O. Häberlen, A. Lidow, C. L. Tsai, T. Ueda, Y. Uemoto, Y. F. Wu, *IEEE Trans. Electron Devices* **2017**, *64*, 779.
[67] A. Ozbek, X. L. Dean-Ben, D. Razansky, *Opto-Acoustic Methods and Applications* **2013**, *12*, 88001.